



Article

# Investigation of the Outflow and Spreading-Solidification Behaviour of Stratified Molten Metal

Ryo Yokoyama <sup>1,\*</sup>, Masahiro Kondo <sup>2</sup> , Shunichi Suzuki <sup>1</sup>, Masaru Harada <sup>3</sup> and Koji Okamoto <sup>4</sup>

- <sup>1</sup> Department of Nuclear Engineering and Management, The University of Tokyo, 7-3-1 Hongo, Bunkyo-ku, Tokyo 113-8656, Japan; s\_suzuki@n.t.u-tokyo.ac.jp
- <sup>2</sup> National Institute of Advanced Industrial Science and Technology (AIST), Central 2, 1-1-1 Umezono, Tsukuba 305-8568, Japan; kondo.masahiro@aist.go.jp
- <sup>3</sup> Materials and Chemistry Division R&D Department, TEPCO Research Institute, 4-1 Egasaki-cho, Tsurumi-ku, Yokohama 230-0002, Japan; harada.masaru@tepcoco.jp
- <sup>4</sup> Nuclear Professional School, The University of Tokyo, 2-22 Shirakata, Tokai-mura 319-188, Japan; okamoto@n.t.u-tokyo.ac.jp
- \* Correspondence: yokoyama@vis.t.u-tokyo.ac.jp

**Abstract:** The spreading-solidification behaviour of the stratified molten metals was investigated. This is important in understanding the practical fuel debris distribution spread and solidified in the primary containment vessel (PCV) of Fukushima Daiichi Nuclear Power Plants (1F NPPs). In this study, the effect of outflow diameter on the material distribution before discharging was studied both experimentally and numerically. The two simulant metals were chosen so that the density ratio could be similar to the practical fuel and structure elements of the plant. They were arranged in a vessel and discharged on a receiving plate. The spreading experiments were performed using various outlet diameters with a density and reverse density stratification arrangement. After the experiment, X-ray analysis was performed to evaluate the material distribution in the solidified material. Moreover, a numerical analysis was performed to reveal the mechanisms that affect the material distribution after solidification. As a result, the low-density metal accumulated at the centre region regardless of the outlet diameters in the density stratification. In contrast, the outlet diameters affected the material distribution in the reverse density stratification because they affected the material outflow order. These findings may help increase our understanding of the fuel debris distribution in 1F NPPs.

**Keywords:** molten metal spreading; severe accident; fuel debris; particle method; stratification; decommissioning; Fukushima Daiichi nuclear power plants



**Citation:** Yokoyama, R.; Kondo, M.; Suzuki, S.; Harada, M.; Okamoto, K. Investigation of the Outflow and Spreading-Solidification Behaviour of Stratified Molten Metal. *J. Nucl. Eng.* **2021**, *2*, 168–189. <https://doi.org/10.3390/jne2020017>

Academic Editor: Jan Willem Coenen

Received: 10 March 2021

Accepted: 6 May 2021

Published: 10 May 2021

**Publisher's Note:** MDPI stays neutral with regard to jurisdictional claims in published maps and institutional affiliations.



**Copyright:** © 2021 by the authors. Licensee MDPI, Basel, Switzerland. This article is an open access article distributed under the terms and conditions of the Creative Commons Attribution (CC BY) license (<https://creativecommons.org/licenses/by/4.0/>).

## 1. Introduction

The retrieval of fuel debris in Fukushima Daiichi Nuclear Power Plants (1F NPPs) is one of the most challenging activities in 1F NPP decommissioning because the fuel debris distribution in the primary containment vessel (PCV) is not sufficiently revealed even though approximately 10 years have passed after the accident. The lack of information makes the retrieval of fuel debris more difficult and complicated. Although the past nuclear severe accidents have provided some information to promote the decommissioning of 1F NPPs, there are obvious differences. Specifically, the differences of the fuel debris in 1F NPPs and Chernobyl NPP are as follows.

- ① A lot of control rod drive mechanisms (CRDMs) were penetrated from the bottom of the reactor pressure vessel (RPV) in 1F NPPs. Thus, a lot of metal-fuel debris might be formed in 1FNPPs compared to Chernobyl [1–3].
- ② A lot of seawater was injected into the PCV in 1F NPPs. Therefore, the sea salt might dissolve into the fuel debris [4], which did not happen in Chernobyl.

Therefore, it is essential to obtain the specific fuel debris characteristics in the 1F NPPs through investigations.

According to Tokyo Electric Power Company Holdings reports (TEPCO HD) [5,6], part of the fuel handle was observed in Unit 2, while a portion of the control rod was detected in Unit 3. These internal investigation results indicate that fuel debris with different characteristics might be generated in each unit. Table 1 is the summary of accident scenarios in 1F NPPs based on the SAMPSON result [7]. The results also indicated that different accident scenarios might happen in 1F NPPs. Predicting the fuel debris distribution by considering accident scenarios is a critical approach to retrieve the fuel debris in 1F NPPs. Understanding the molten corium spreading and solidification phenomena is crucial for evaluating the fuel debris distribution in 1F NPPs because they might determine the initial distribution and further accident progression after reactor pressure vessel (RPV) failure, such as molten core concrete interaction (MCCI).

**Table 1.** Summary of accident scenarios in 1FNPPs [7].

Unit 1 in 1F NPPs	Unit 2 in 1F NPPs	Unit 3 in 1F NPPs
1 h: Stop cooling by IC	70 h: Stop RCIC cooling	41 h: Control rod start melting
5 h: Fuel start melting	78 h: Control rod start melting	42 h: Fuel rod melting
24 h: Open PCV vent system	81 h: Fuel start melting	50 h: Fuel debris fall down onto PCV
25 h: Reactor building is destroyed by explosion	82 h: Corium relocated to lower head	
50 h: PCV shell attack, MCCI	90 h: Degradation of lower head	
	120 h: Corium discharge from RPV	

Even before the 1F NPP accident, there were the following research programs on molten corium spreading. CORINE (CEA, France) [8,9], Green (BNL, USA) [8,10], S3E (KTH, Sweden) [8], SPREAD (Hitachi, Japan) [8,11], KATS (KIT, Germany) [8,12], EKOCATS (KIT) [13,14], COMAS (Siempelkamp, Germany) [8,15], FARO (JRC, Italy) [8,16], and VULCANO (CEA) [8,17] are experimental programs using simulant materials. However, these experiments did not consider the downward jet flow of the molten simulants and their interaction with the lower structures, although such phenomena could happen in 1F NPPs.

Therefore, experimental programs considering the above issues were conducted after the 1F NPP accident in small scale experiments [18–22]. Ogura et al. [18,19] conducted experiments using a high-speed thermocamera to explore the spreading and solidification behaviour, focusing on the relationship between the outlet diameters and the falling height under both dry/wet surface conditions. Furthermore, Yokoyama et al. [23] examined the effect of the amount of molten metal and outlet diameters on the melt spreading behaviour.

The majority of the experimental programs before and after the 1F NPP accident used simulant materials that were well mixed. However, in practical accidents, molten corium stratifies between fuel and structural components due to density differences [24,25]. If the material distribution in the fuel debris were not homogeneous, it would affect the selection of the cutting devices [26], aerosol removal management [26,27], and even re-criticality management for fuel debris retrieval [28].

Numerical simulation is useful as well as experiments to understand the melt spreading behaviour. Particle methods [29,30] are useful in capturing the material flows during melt spreading. The moving particle full-implicit (MPFI) method [31–33] is one such particle method recently developed by Kondo [31]. Since the MPFI method ensures the conservation of angular momentum, it can capture the rotational motion of the solid. This aspect is vital because the molten metal spreading phenomenon is quite complicated due to the phase change among the solid-state, liquid state, and liquid-solid-state.

In this study, the outflow and the spreading-solidification behaviour of the stratified molten metal discharged downward from the outlet was investigated. The molten metal spreading experiments considering the stratifications were performed under the various outlet diameters. The solidified material distribution depending on the outlet diameters was studied with the density stratification and the reverse density stratification conditions, respectively. The investigation was done both experimentally and numerically.

In Section 2, the experiment set-up is described, and the experimental results including X-ray analysis are shown in Section 3. In Section 4, the MPFI method [31–33], which is the numerical method adopted in this study, is presented. The simulation results are shown in Section 5. Moreover, the mechanism with respect to the spreading-solidification behaviour is discussed in Section 6. Finally, the conclusion of this study is shown in Section 7.

## 2. Experimental Set-Up

In this study, the spreading-solidification behaviour of the stratified molten metal discharged downward from the outlet was observed. After solidification, X-ray analysis was performed to visualize the material distribution.

A schematic of the test facility is shown in Figure 1. The test facility consists of a vessel to heat the simulants and a receiving plate to observe the melt spreading-solidification behaviour. Furthermore, a detailed image of the test vessel is shown in Figure 2, produced from stainless steel (SS), and a thermocouple (TC) measures the simulant temperature 20 mm from the bottom. The receiving plate is also made of SS. It is a square shape with a length and width of 20 cm and a 5 mm thickness.

In this study, two simulant materials, U-alloy47 and U-alloy109, were adopted such that their density ratio was closer to that between the fuel components and the structural components. U-alloy47 has a higher density for the fuel components, and U-alloy109 has a lower density for the structural components. The detailed characteristics of both simulants are summarized in Table 2. These simulants were arranged in the vessel shown in Figure 3. In this study, two stratification patterns were adopted. One is density stratification, in which the high-density simulant is prepared under the low-density simulant. The other is reverse density stratification, in which the low-density simulant is organized under the high-density simulant.

**Table 2.** Simulant material properties.

	High-Density (U-alloy47)	Low-Density (U-alloy109)
Density, $\rho$ (kg/m <sup>3</sup> )	9360	8640
Composition, (at.%)	Bi44.7, Pb22.6, Sn12.3, Cd5.3, In17.1	Bi66, In34
Melting Temperature, $T_m$ (°C)	47	109
Thermal Conductivity, $k$ (W/m K)	36	30
Specific Heat, $C_p$ (J/kg K)	190	250
Viscosity, $\mu$ (Pa s)	$3.3 \times 10^{-4}$	$6.4 \times 10^{-4}$
Thermal expansion coefficient, $\beta$ (K <sup>-1</sup> )	$2.4 \times 10^{-5}$	$3.9 \times 10^{-5}$

After arranging the stratified simulants, the vessel was heated to 200 °C with the ribbon heater and the temperature controller. When the simulant temperatures in the vessel reached 170 °C, the plug was pulled out, and the liquefied molten metals flew out from the vessel and spread on the receiving plate. The spreading and solidification behaviours were recorded using a video camera at 60 fps (HANDYCAM HDR-CX485, SONY, Tokyo, Japan).

After the spreading-solidification experiment, the solidified materials were removed from the plate, and the upper surface and the surface detached from the plate were analysed with an X-ray analytical microscope (XGT-7200, HORIBA, Japan). Figure 4 illustrates the X-ray analysis procedure where two types of analysis were conducted. A mapping analysis visualized the element distribution derived from the high-density simulant in the solidified metal. X-rays were irradiated for the entire area of the solidified metal, and the concentration distribution of the substances was pictured. A point analysis was used to obtain quantitative data on the atomic percentage of substances derived from the high-density simulant. In the point analysis, X-rays are irradiated at five points from the centre to the edge. In this analysis, since the measurement points on the surface are targeted, X-ray analytical microscope can measure regardless of the sample shape. The experiments and X-ray analysis were performed twice to confirm the validity of the experiment results. The experimental conditions are summarized in Table 3. In this experimental condition,

the Rayleigh number ( $Ra$ ) of the molten metal was less than critical  $Ra$  number and the experiments were quickly carried out. Therefore, it is expected that the stratification was maintained in the vessel before discharging.

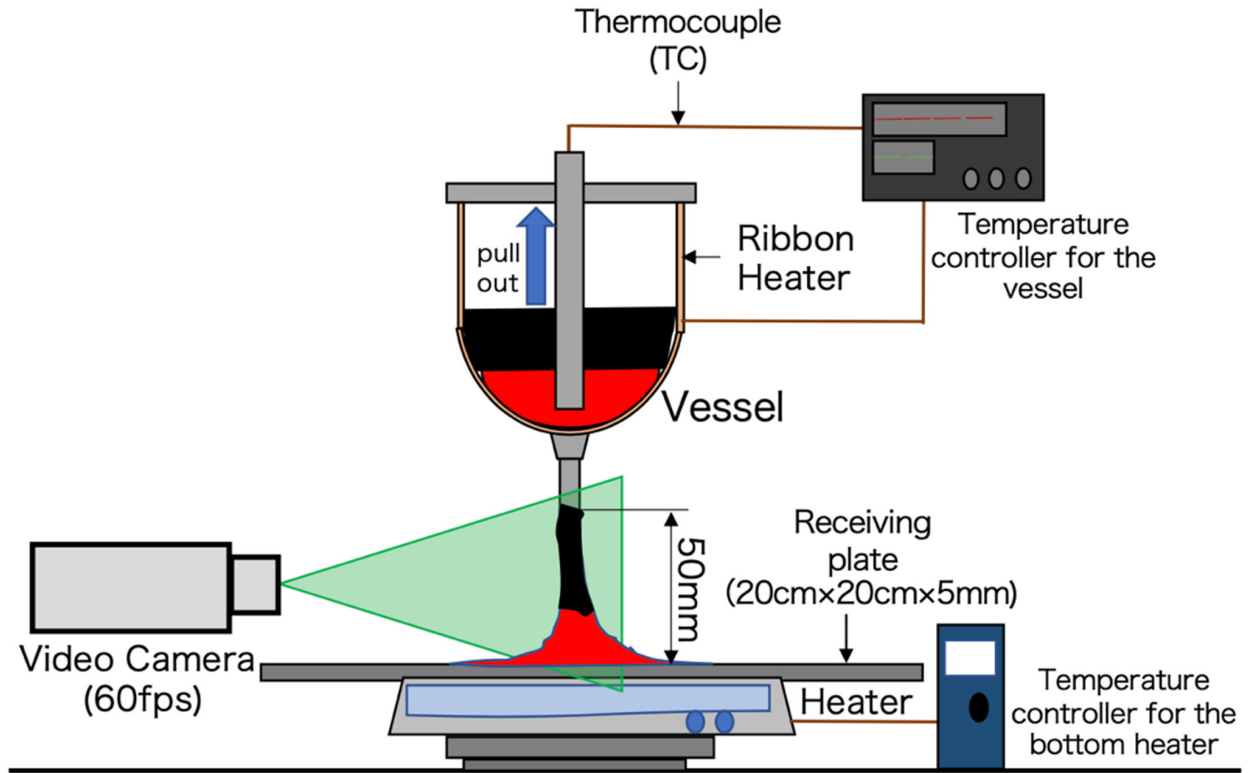


Figure 1. Schematic illustration of the test facility.

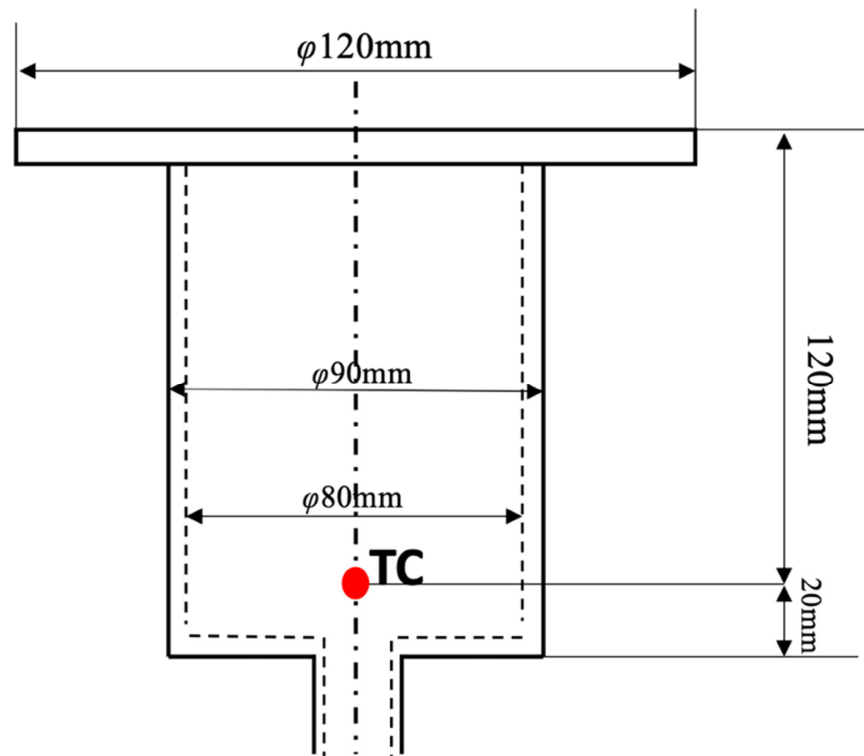


Figure 2. Details of the test vessel and TC location.

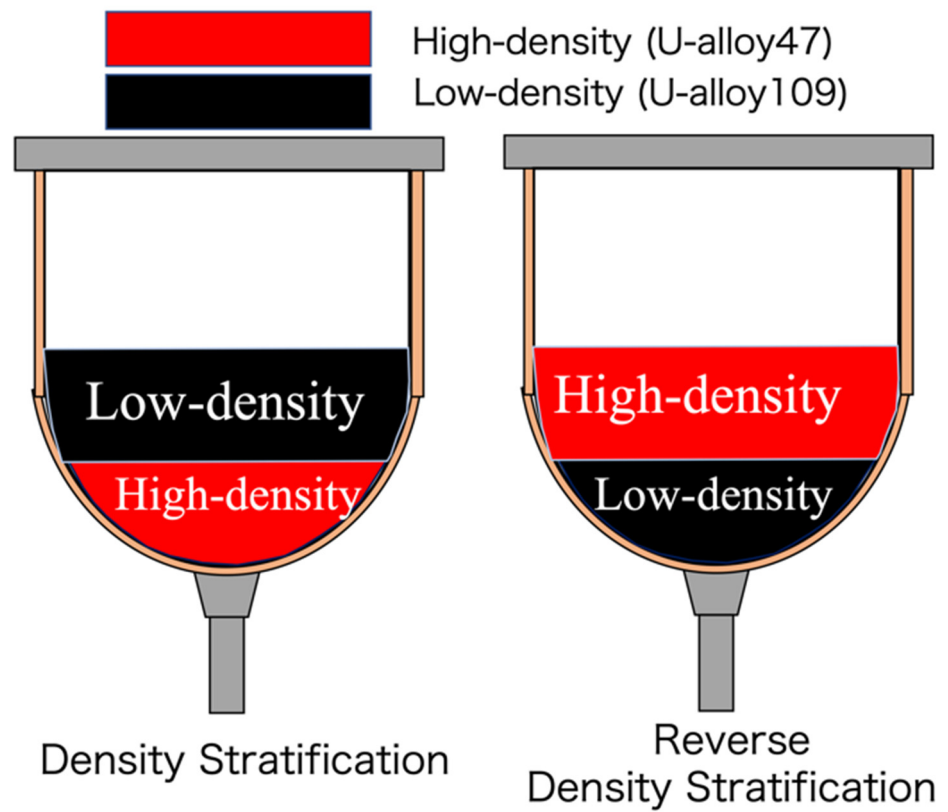


Figure 3. The arrangement of the simulants in the vessel.

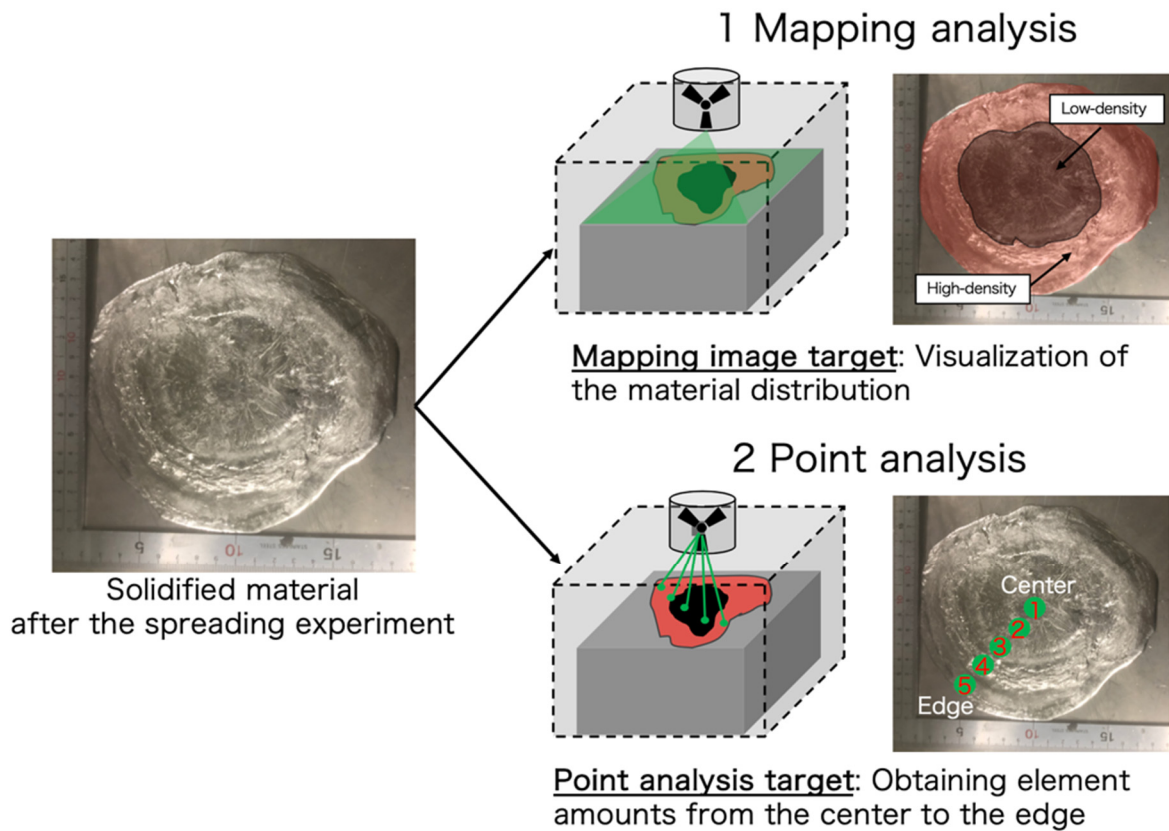


Figure 4. Procedure of the X-ray analysis.

**Table 3.** Summary on the experiment conditions.

	Values
Sample amount, $M$ (g)	200
Sample temperature, $T$ ( $^{\circ}\text{C}$ )	170
Outlet diameter, $D$ (mm)	3,5,7,9
Falling height from vessel to receiving plate, $H$ (mm)	50
Environmental temperature, $T_e$ ( $^{\circ}\text{C}$ )	$30 \pm 0.5$
Receiving plate temperature, $T_r$ ( $^{\circ}\text{C}$ )	$25 \pm 1.0$
Rayleigh number, $Ra$ (-)	Approximately 1000

**3. Experimental Results**

*3.1. X-ray Analysis Results under the Density Stratification Condition*

The mapping image analysis results on the density stratification are depicted in Figure 5. Pb was chosen to trace the migration of the high-density simulant. The white region corresponds to the high concentration of Pb. The mapping results demonstrated that high-density materials accumulated around the edge region on the front side with all outlet diameters tested. On the backside, the high-density materials tend to spread throughout the entire area regardless of outlet diameter.

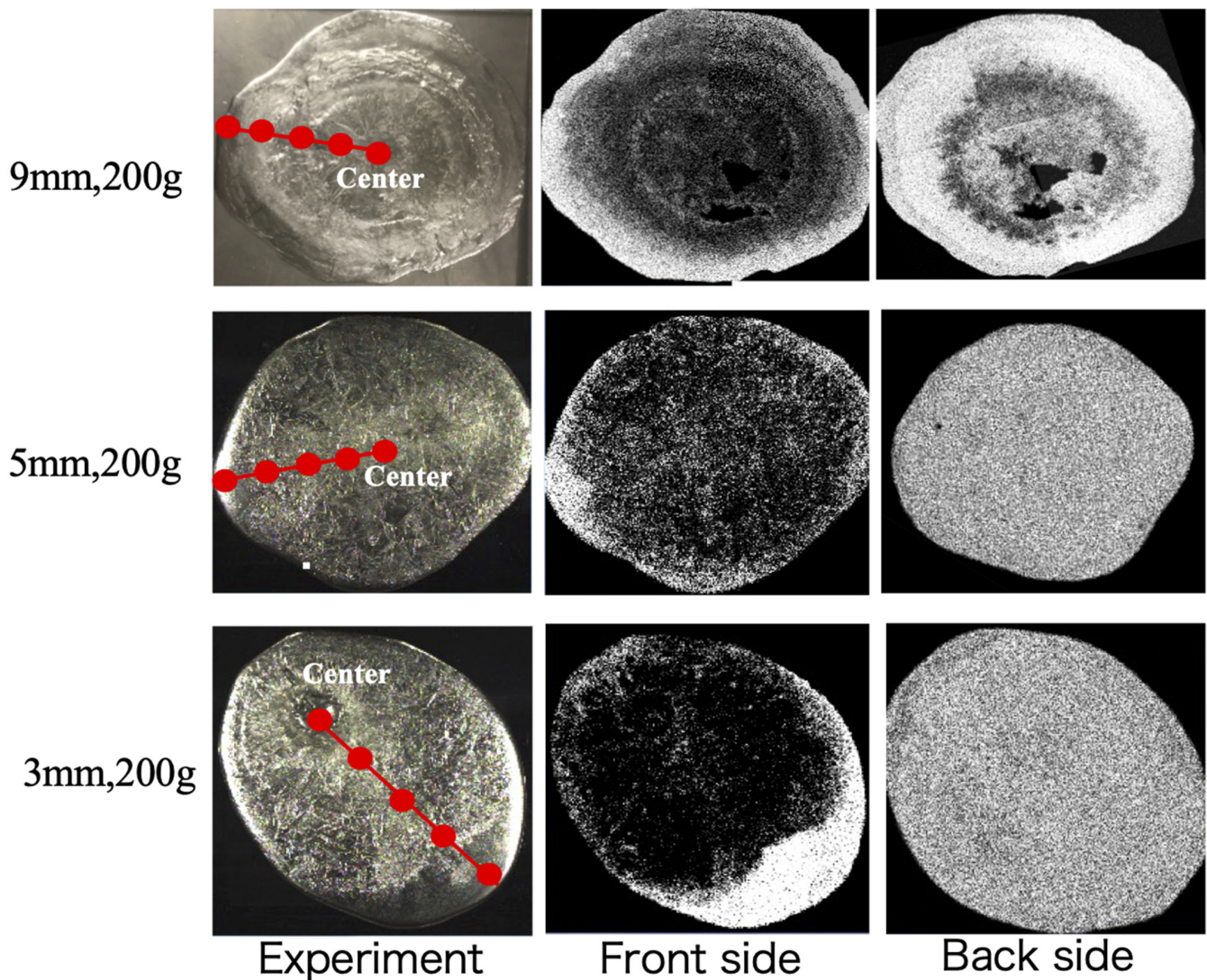


**Figure 5.** Mapping image analysis results in the density stratification.

The point analysis results on Pb distribution are shown in Figure 6. The horizontal axis represents the distance from the centre to the edge shown in Figure 5. The vertical axis represents Pb ratio obtained from the analysis at the measurement point. As a result, the Pb ratio gradually increased as it approached the edge region on the front side. On the other hand, Pb was distributed in the entire area on the backside.

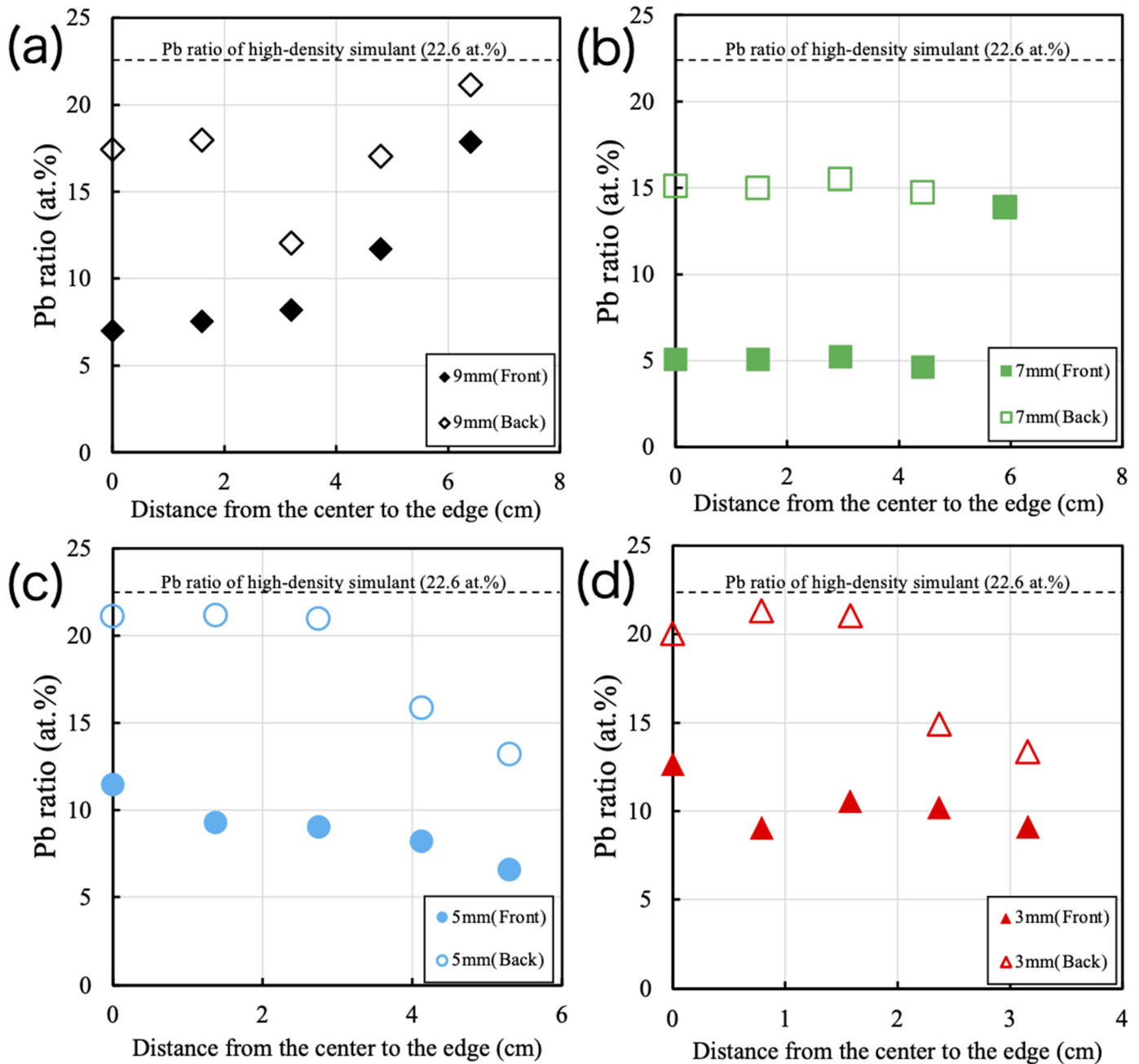


**Figure 6.** Pb distribution in the solidified metal under the density stratification (a) 9 mm outlet, (b) 7 mm outlet, (c) 5 mm outlet, (d) 3 mm outlet.

### 3.2. X-ray Analysis Results under the Reverse Density Stratification Condition

Figure 7 presents the mapping image analysis results on the reverse density stratification. It was determined that the substance distribution was remarkably affected by the outlet diameters. Unlike the results obtained with the density stratification condition shown in Figure 5, the backside distribution was not uniform. It is considered that the

velocity of the melt due to the outlet diameters influenced the heterogeneous distribution. Specifically, the high-density simulant tended to accumulate around the centre with 5 mm and 3 mm outlets. In contrast, the opposite tendency i.e., edge accumulation was detected in the case with 9 mm.

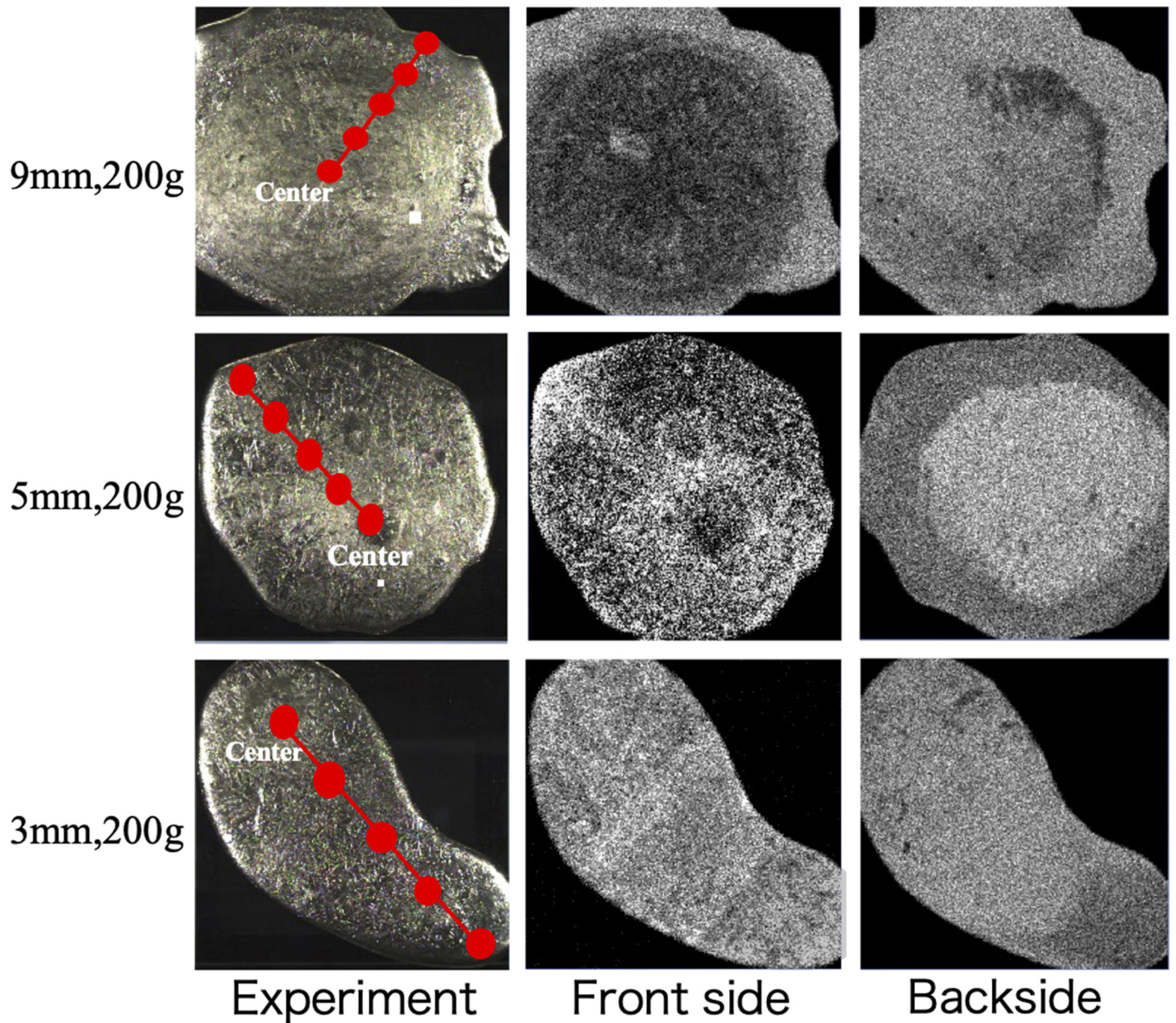
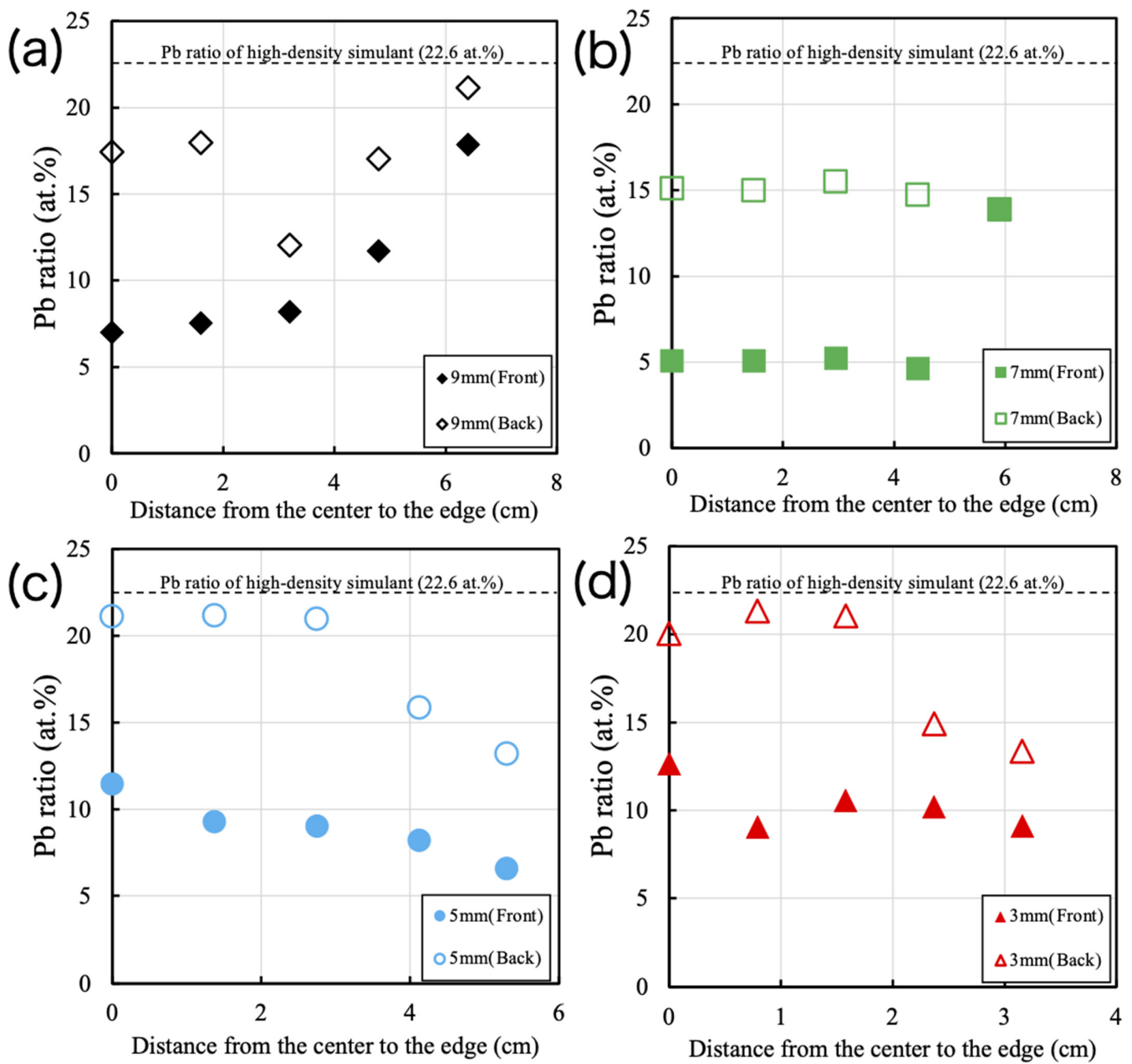


Figure 7. Mapping image analysis results in the reverse density stratification.

The point analysis results on the Pb distribution under the reverse density stratification condition are shown in Figure 8. For large outlets, i.e., 9 mm and 7 mm, larger amounts of Pb tended to be observed at the edge. In contrast, for small outlets, i.e., 5 mm and 3 mm, the Pb distribution was detected near the centre. These findings signified that the outlet difference affected the eventual material distribution.



**Figure 8.** Pb distribution in the solidified metal under the reverse density stratification (a) 9 mm outlet, (b) 7 mm outlet, (c) 5 mm outlet, (d) 3 mm outlet.

#### 4. Numerical Method

##### 4.1. Basic MPFI Method

For the numerical simulation, the MPFI method [31–33] was applied, which is one of the particle methods [29,30]. Since the method has thermodynamic consistency, a stable calculation can be conducted. In the MPFI method, the following Navier-Stokes (N-S) equation is adopted to simulate the incompressible free-surface flow. The equation is expressed as:

$$\rho \frac{du_i}{dt} = \frac{\partial}{\partial x_i} \mu \dot{\epsilon}_{ij} + \frac{\partial}{\partial x_i} P_i + \rho g_i, \tag{1}$$

where  $g, P, u, \rho, \mu$  and  $\varepsilon$  are gravity acceleration, pressure, velocity, fluid density, fluid viscosity, and strain rate, respectively. The first term on the right-hand side is the viscosity term and the second-hand term is the pressure term. Here, the pressure is expressed as:

$$P = \left( -\lambda \dot{\varepsilon}_{kk} + \kappa \frac{\rho_k - \rho_0}{\rho_0} \right). \tag{2}$$

where  $\lambda$  and  $\kappa$  are bulk viscosity and bulk modules, respectively. In this study,  $\lambda$  and  $\kappa$  were set to  $1.0 \times 10^{10}$  and  $1.0 \times 10^9$ , respectively. When these values are set large enough, they have almost no effect to the calculation. The first term on the right-hand side is bulk viscosity term and the second-hand term is bulk strain term. In particle methods, the governing equations are replaced by particle interaction forces. To save computational costs, the particle interactions are limited in a finite range using an effective radius and a weight function. In the MPFI method, the particle interaction models for gradient, divergence, and Laplacian operators are formulated as:

$$\nabla \phi = \sum_j (\phi^j + \phi^i) r_r^{ij} \frac{w^{ij}}{d^{ij}}, \tag{3}$$

$$\nabla \cdot A = \sum_j (A^j - A^i) r_r^{ij} \frac{w^{ij}}{d^{ij}}, \tag{4}$$

$$\nabla^2 \phi = \sum_j (\phi^j - \phi^i) \frac{w^{ij}}{d^{ij}}, \tag{5}$$

where  $\phi, A, r^{ij}$ , and  $d^{ij}$  are an arbitrary scalar, an arbitrary vector, the relative position between particles  $i$  and  $j$ , the particle distance, respectively.  $w^{ij}$  is a differential of the weight function with respect to particle distance  $d^{ij}$  defined as:

$$w^{ij} = \begin{cases} (r_e - d^{ij}) & (d^{ij} < r_e) \\ 0 & (d^{ij} > r_e) \end{cases} \tag{6}$$

In this study, the effective radius,  $r_e = 2.0l_0$ , was adopted, where  $l_0$  is the initial particle spacing. When Equation (1) is discretized using the particle interaction models (Equations (3)–(5)), the force acting on the particle is expressed as:

$$\frac{du_i}{dt} = 2\mu \sum_j \left( u_r^j - u_r^i - \frac{\omega_p^j + \omega_p^i}{2} r_q^{ij} \varepsilon_{pqr} \right) \frac{w^{ij}}{d^{ij}} - \lambda \sum_j (\dot{\varepsilon}^j + \dot{\varepsilon}^i) r_r^{ij} \frac{w^{ij}}{d^{ij}} + \rho g, \tag{7}$$

where:

$$P^i = -\lambda \sum_j (u^j - u^i) r_r^{ij} \frac{w^{ij}}{d^{ij}} + \kappa \frac{n_i - n_0}{n_0}, \tag{8}$$

$$\sum_j \left( u_r^j - u_r^i - \omega_p^i r_q^{ij} \varepsilon_{pqr} \right) r_s^{ij} \varepsilon_{rst} \frac{w^{ij}}{d^{ij}} \Delta t = 0. \tag{9}$$

Here, an angular velocity  $\omega$  and an equation (Equation (9)) are additionally introduced to conserve angular momentum by subtracting the rotational element [33]. Equations (7)–(9) are linear matrix equations including unknown values of velocity  $u$ , angular velocity  $\omega$ , and pressure  $P$ . Since its coefficient matrix is symmetric, it can be solved by the conjugated residual method.

#### 4.2. Heat Transfer Model

In this study, the heat transfer model and phase change model were introduced based on previous works [34–40]. Heat transfer calculations are essential to simulate

melting-solidification behaviour. The temperature field is computed with the energy conservation equation:

$$\frac{DH}{Dt} = k\nabla^2 T + Q, \tag{10}$$

where  $H$ ,  $k$ ,  $T$ , and  $Q$  are enthalpy per unit volume, thermal conductivity, temperature, and the heat source, respectively. The first term of the right-hand side is the temperature gradient and the second-hand term is the heat input term, respectively. The equation is discretized with the Laplacian operator (Equation (5)) as:

$$\frac{DH_i}{Dt} = \sum_j k_{ij}(T^j - T^i) \frac{w^{ij}}{d_{ij}} + Q. \tag{11}$$

The parameter  $k_{ij}$  is the thermal conductivity between particle  $i$  and particle  $j$  given as [38,40]:

$$k_{ij} = \frac{2k_i k_j}{k_i + k_j}. \tag{12}$$

In this study, the heat transfer coefficient between the solid and the liquid is calculated based on the Nusselt number on the flat surface. Thus:

$$Nu = 0.664 Re^{\frac{1}{2}} Pr^{\frac{1}{3}} \left( Re < 3.2 \times 10^5 \right), \tag{13}$$

$$Nu = 0.037 Re^{0.08} Pr^{1/3} \left( Re > 3.2 \times 10^5 \right), \tag{14}$$

$$h = \frac{Nu k_i}{L}, \tag{15}$$

where  $h$ ,  $L$ ,  $Re$ , and  $Pr$  are the heat transfer coefficient, the representative length, which is the spread length of the molten metal, Reynolds number, and Prandtl number, respectively. The energy conservation equation between the solid and the liquid can be formulated as follows using this heat transfer coefficient:

$$\frac{DH_i}{Dt} = \sum_j hL(T^j - T^i) \frac{w^{ij}}{d_{ij}} + Q. \tag{16}$$

In addition, the heat loss due to radiation from the free surface is considered. The radiation heat loss is simply modelled as heat removal from the free surface particles based on Stephan-Boltzmann's law:

$$q_{radiation} = \sigma \epsilon A (T^4 - T_e^4), \tag{17}$$

where  $\sigma$ ,  $\epsilon$ ,  $A$ ,  $q_{radiation}$ , and  $T_e$  denote the Stephan-Boltzmann constant, emissivity, surface area of the particle, heat flux from radiation, and environmental temperature, respectively. The energy conservation equation for the free surface particles can be expressed as:

$$\frac{DH_i}{Dt} = \sum_j k_{ij}(T^j - T^i) \frac{w^{ij}}{d_{ij}} - \frac{q_{radiation}}{l}, \tag{18}$$

where  $l$  denotes the particle diameter.

#### 4.3. Phase Change Model

The phase change is a key factor for simulating the melting-solidification behaviours of the molten metal. In this study, phase changes are expressed by changing the particle

viscosity in accordance with its enthalpy and solid fraction. The temperature  $T$  and the solid fraction  $\gamma$  are calculated by using the enthalpy as:

$$T = \begin{cases} T_m + \frac{h-h_0}{\rho C_{ps}} & (h < h_0) \\ T_m + \frac{h-h_0}{\rho C_{pm}} & (h_0 < h < h_1) \\ T_m + \frac{h_1-h_0}{\rho C_{pm}} + \frac{h-h_1}{\rho C_{pl}} & (h_1 < h) \end{cases} , \quad (19)$$

$$\gamma = \begin{cases} 1 & (h < h_0) \\ \frac{h_1-h}{h_1-h_0} & (h_0 < h < h_1) \\ 0 & (h_1 < h) \end{cases} . \quad (20)$$

where  $C_{ps}$ ,  $C_{pm}$ ,  $C_{pl}$ ,  $h_0$ ,  $h_1$ , and  $T_m$  are specific heat for solid state, specific heat at the melting point, specific heat for liquid, solidifying enthalpy, liquefying enthalpy, and melting point, respectively. When  $\gamma = 0$ , the particle is in a complete fluid state; when  $\gamma = 1$ , the particle is in a complete solid-state; and when  $0 < \gamma < 1$ , the particle is a mixture of solid-liquid states.

The reproduction of solidification is essential in this study. Ramacciottii [41] proposed an empirical viscosity model that is a function of the solid fraction. In this model, the viscosity was increased up to the immobilization solid fraction called the “critical solid fraction”, and the viscosity was set as a constant value above the critical solid fraction to stop flowing. This empirical equation has been widely used to reproduce melting-solidification behaviour [34–40]. However, it was suggested that the critical solid fraction for flowing is significantly affected by ① the shear rate of the fluid, ② the cooling ratio, and ③ the material characteristics [42,43]. Therefore, the critical solid fraction should be set in accordance with the expected flow rate because the flow rate changes depending on the outlet diameters:

$$(Large\ outlet : outlet\ 9\ and\ 7mm) \begin{cases} \mu = \mu_0 exp(2.5C\gamma) & (0 < \gamma < 0.30) \\ \mu = 1 \times 10^5 & (0.30 \leq \gamma < 1) \end{cases} , \quad (21)$$

$$(Small\ outlet : outlet\ 5\ and\ 3mm) \begin{cases} \mu = \mu_0 exp(2.5C\gamma) & (0 < \gamma < 0.50) \\ \mu = 1 \times 10^5 & (0.50 \leq \gamma < 1) \end{cases} , \quad (22)$$

where  $\mu_0$  and  $C$  are the viscosity coefficient and a constant value, respectively, which is experimentally determined. In general, the  $C$  value is set from 4 to 8. In this study,  $C = 6.4$  was adopted, which was determined by previous work [38].

The calculation geometry is depicted in Figure 9, where the red particle corresponds to the high-density fluid, and the black particle corresponds to the low-density fluid. The detailed calculation conditions are listed in Table 4. Three different particle diameters (0.007, 0.009 m, and 0.012 m) were performed for the sensitivity analysis. The results with 0.012 m could not reproduce the experimental results. Since the calculation with 0009 m could reproduce the experimental results with reasonable calculation time, the particle diameter, 0.009 m, was selected in this study.

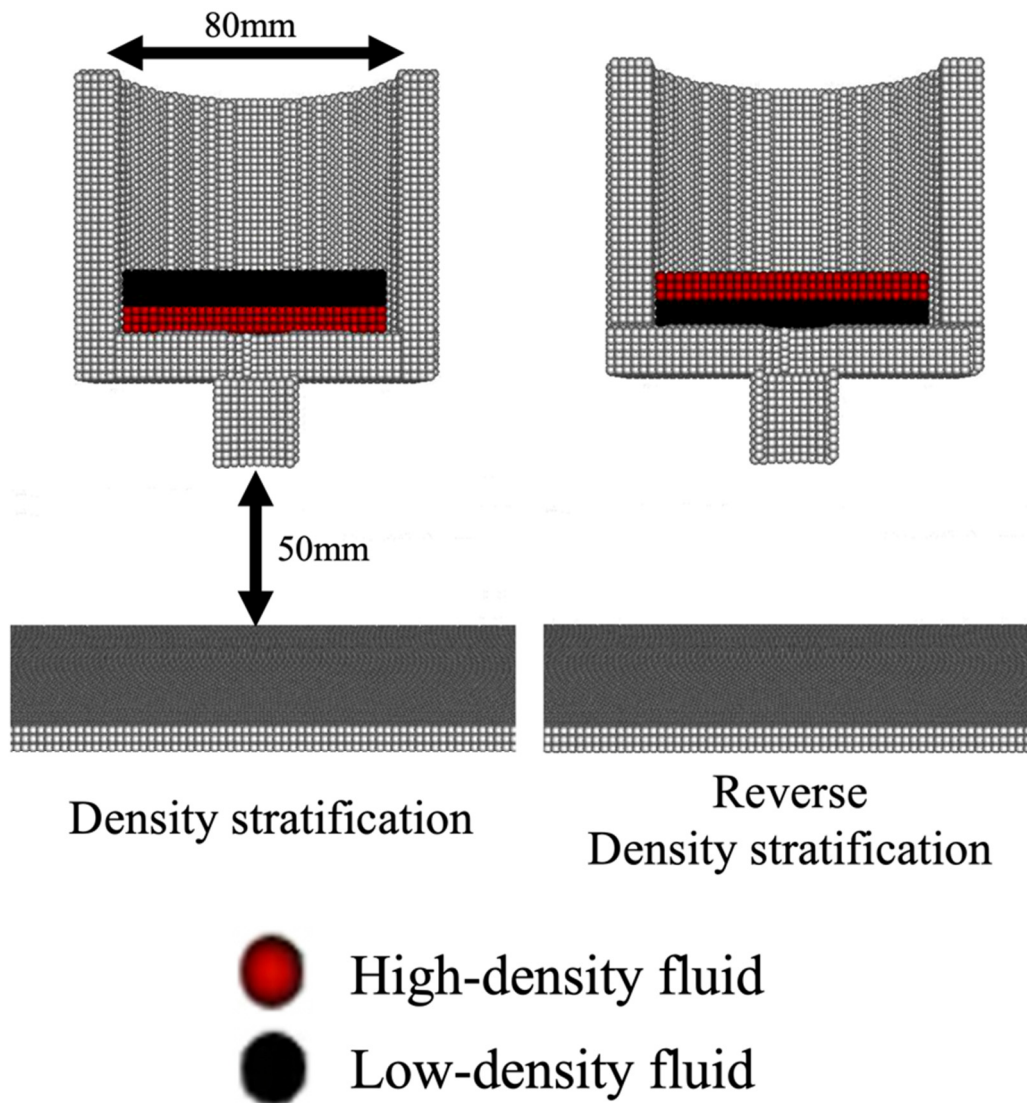


Figure 9. Simulation geometry with the different stratification conditions.

Table 4. Calculation conditions for the simulation.

	High-Density Fluid	Low-Density Fluid
Particle spacing (mm)		0.009
Impact radius (mm)		0.017
Sample amount, $M$ (g)	100	100
Nozzle diameter, $D$ (mm)	3,5,9	3,5,9
Specific heats for the solid and liquid, $C_{ps}, C_{pl}$ (J/kg K)	190	250
Melting point, $T_m$ (°C)	60	90
Thermal conductivity, $k$ (W/m K)	36	30
Latent heat, $h_1 - h_0$ (J/kg)	25,000	30,000
Initial viscosity (170 °C), $\mu_0$ (Pa s)	$3.3 \times 10^{-4}$	$6.3 \times 10^{-4}$
Stephan-Boltzmann constant, $\sigma$		$5.67 \times 10^{-8}$
Emissivity, $\epsilon$		0.15
Environmental temperature, $T_e$ (°C)		30

## 5. Numerical Simulation Results

### 5.1. Simulation Results in the Density Stratification

Snapshots of the molten metal spreading behaviour in density stratification with a 9 mm outlet and 3 mm outlet are depicted in Figure 10a,b, respectively. Although the flow rate differed depending upon the outlet diameters, the low-density fluid flew out later and accumulated on the high-density fluid in both cases.

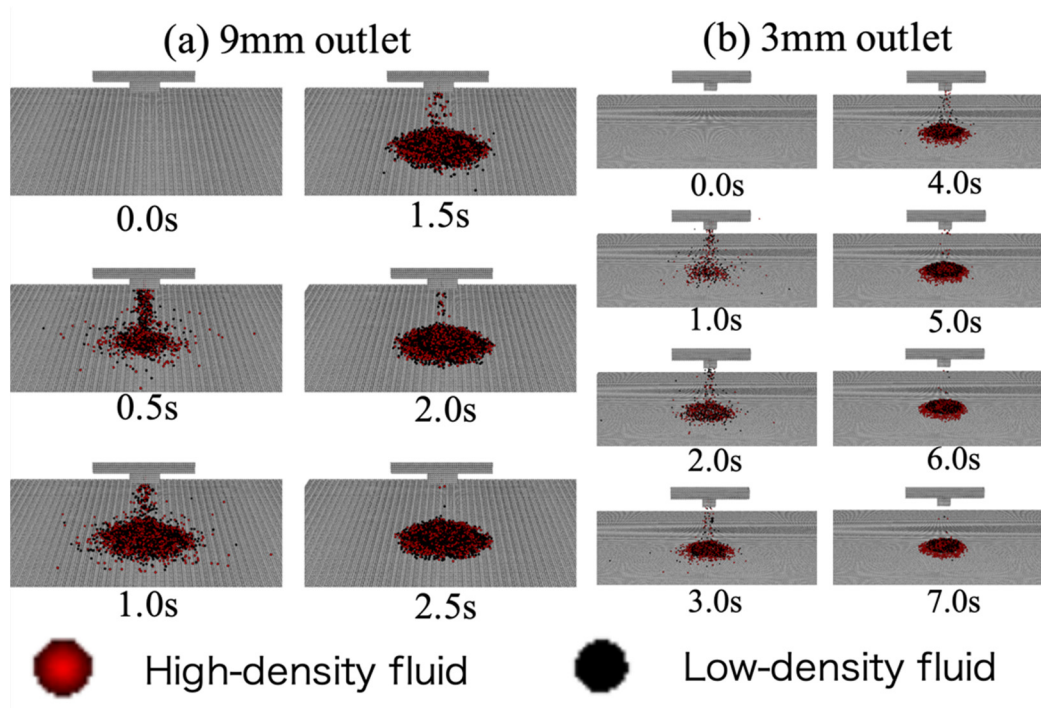


**Figure 10.** Snapshots of the spreading behaviour with different outlet in the case of the density stratification (a) 9 mm outlet, (b) 3 mm outlet.

The material distribution after solidification with different outlet diameters is summarized in Figure 11. Low-density fluid particles accumulated around the centre region and high-density fluid particles were deposited around the edge of the front surface. On the backside, many high-density fluid particles occupied the entire region regardless of the outlet sizes. The simulation results qualitatively agreed with the mapping image in Figure 5 obtained via experiments.

### 5.2. Simulation Results in the Reverse Density Stratification

The spreading behaviour in the reverse density stratification with 9 mm and 3 mm outlets is shown in Figure 12a,b, respectively. The material distribution after solidification with various outlets in reverse density stratification is summarized in Figure 13. In the 9 mm outlet case, high-density fluid particles accumulated at the edge on both the front and the back sides. In contrast, the high-density fluid particles accumulated around the central region on both sides in the 5 mm and 3 mm outlet cases. The simulation results on the outflow rate with the 9 mm outlet and 3 mm outlet are shown in Figure 14a,b, respectively. The outlet scale controlled the outflow order of the reverse stratified fluid. The high-density fluid was sucked into the outlet, and the cumulative outflow rate of the high-density fluid exceeded the low-density fluid at approximately 60% in the 9 mm outlet. In contrast, there was no overtaking in the 3 mm outlet. According to the Koyaguchi experiment [44] and Blake and Ivey's analysis [45], the phenomenon was likely derived from the inertia effect.

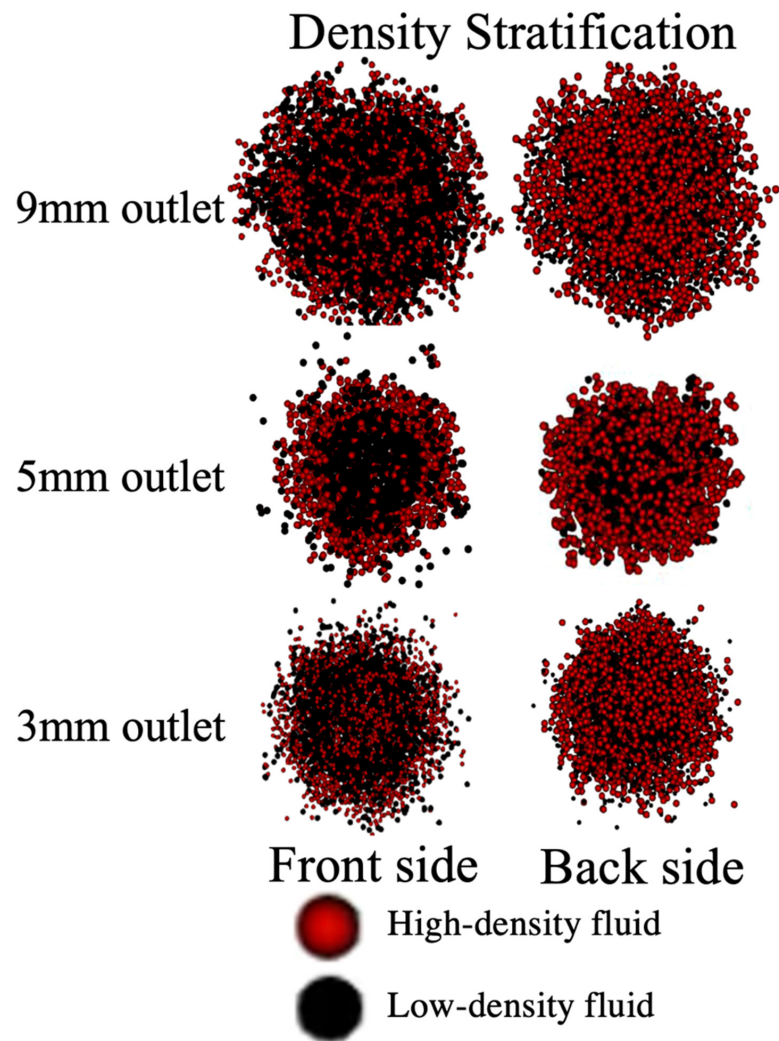


**Figure 11.** Summary of the material distributions after the solidification with different outlet in the case of the density stratification.

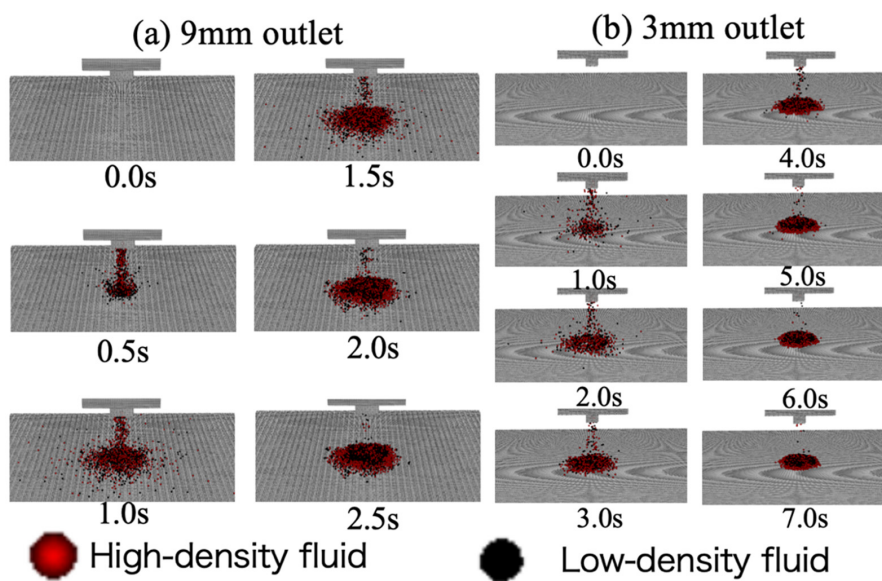


**Figure 12.** Snapshots of the spreading behaviour with different outlets in the case of the reverse density stratification (a) 9 mm outlet, (b) 3 mm outlet.

### Reverse Density Stratification

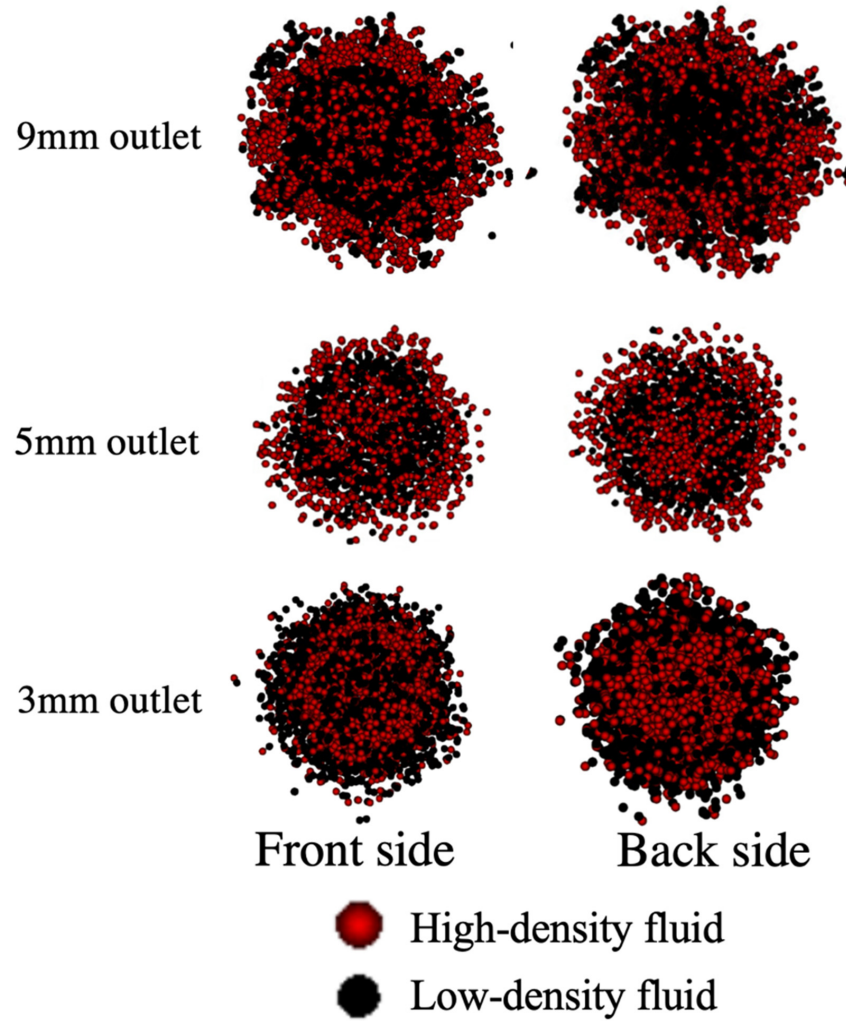


Figure 13. Summary on the material distribution after the solidification with different outlet in the case of the reverse density stratification.

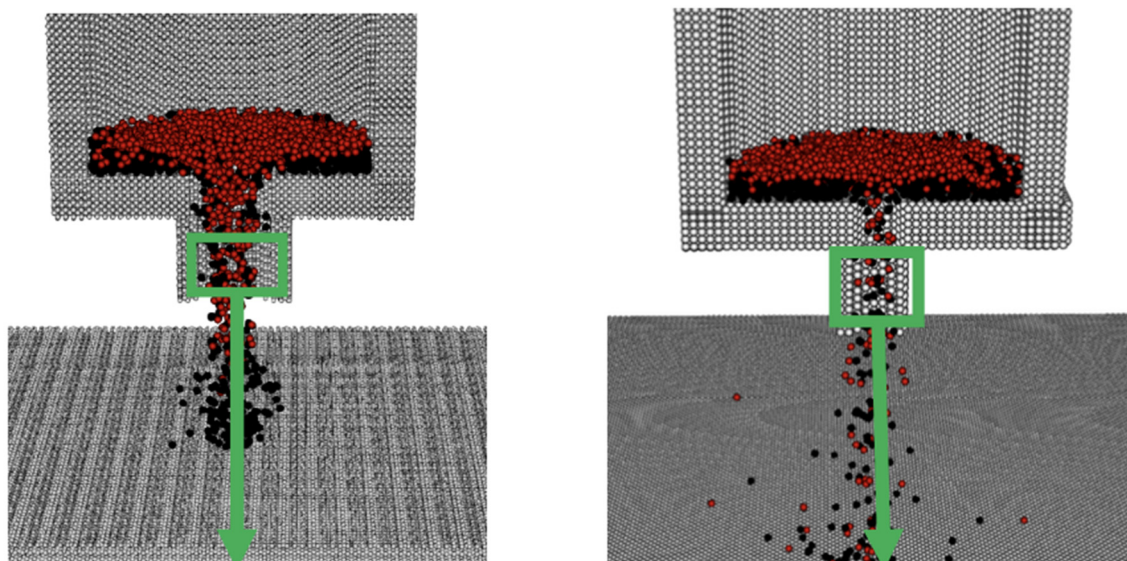


Figure 14. Cont.

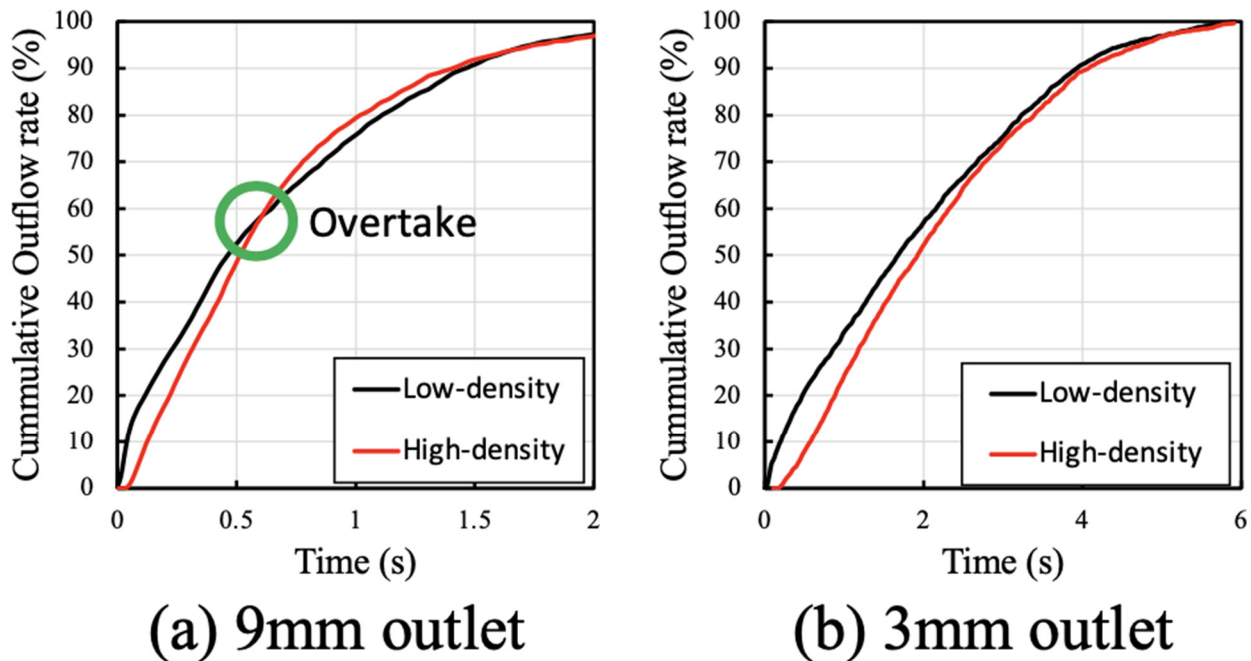


Figure 14. Outlet effect on the outflow rate in the case of the reverse density stratification.

## 6. Discussion

### 6.1. Summary of the Spreading and Deposition Progression of the Stratified Material

Based on both the experimental and the simulation results, the spreading and deposition progression for each stratification condition is summarized. Figure 15 is a schematic summary of the phenomena in this study.

<Density stratification condition>

- ① High-density material was first discharged, spread on the receiving plate, and solidified.
- ② Low-density material spread on the high-density fluid and accumulated around the centre region.
- ③ After solidification, the low-density material was observed only near the centre on the front side.

In the reverse density stratification case, the outflow tendency depended on the outlet diameters.

<Reverse density stratification with large outlet>

- ① A part of the low-density material was discharged and spread on the receiving plate, but shortly thereafter, the high-density material was sucked into the nozzle and preferentially flowed out, and the high-density material spread on the low-density material.
- ② The residual low-density material was deposited on the high-density material.
- ③ On both sides, the low-density material was observed at the edge, and the high-density material was around the centre.

<Reverse density stratification with small outlet>

- ① Most of the low-density material was discharged and deposited on the receiving plate.
- ② High-density material flowed out and accumulated around the centre region.
- ③ After solidification, high-density material accumulated around the centre region, and low-density material accumulated around the edge region.

From the entire results, it was found that the outflow and the spreading-solidification behaviour of the stratified molten metal were depending on the outlet diameters. However, in order to represent the phenomena in 1FNPPs, the scale effect between the present study and 1FNPPs should be taken into consideration. In 1FNPPs, due to the large mass flow rate of the molten metal compared to this study, the inertia effect might be dominant. According to Blake, S. Ivey, GN analysis [39], the large inertia effect induces the large suction effect of the stratified material. Therefore, it is possible that the schematic phenomena shown in Figure 15 occurred in 1FNPPs regardless of the scale effect.

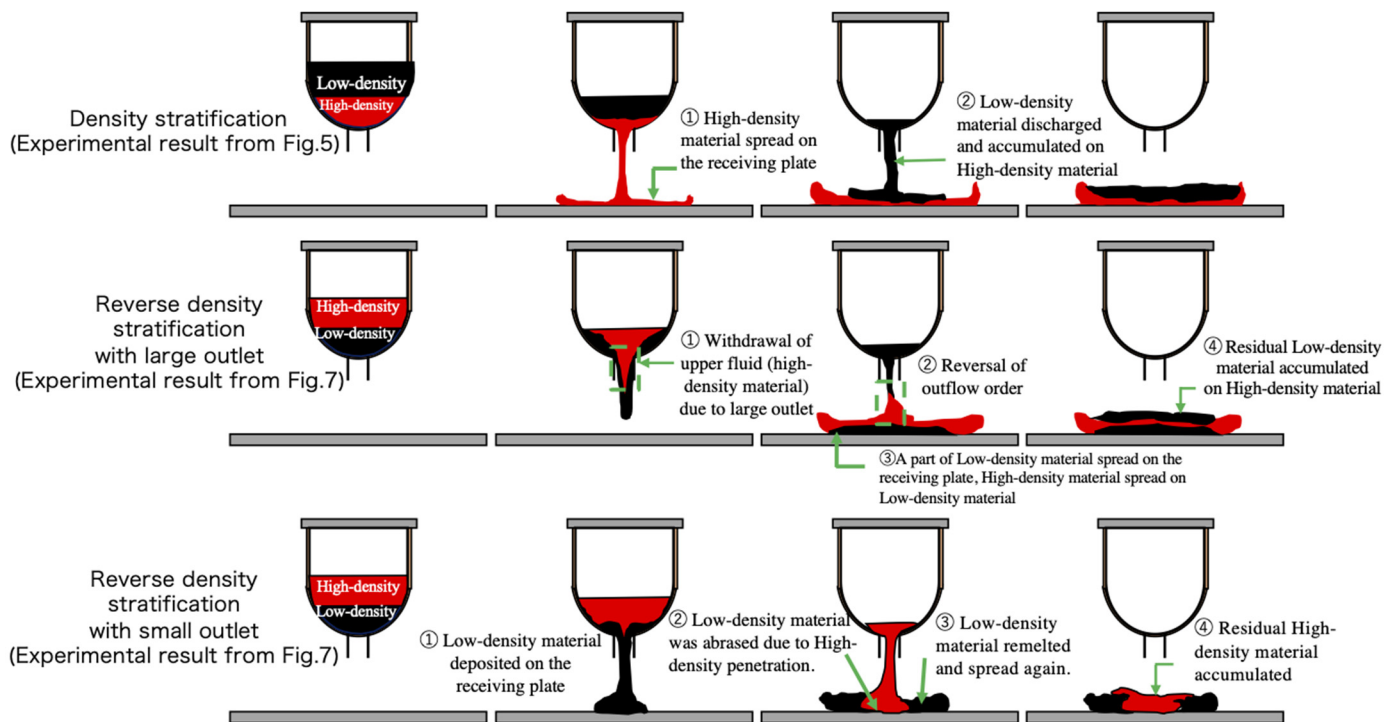


Figure 15. Summary of the spreading and deposition progression.

### 6.2. Comparative Study on the Fuel Debris Distribution between Present Study and the Fuel Debris in 1F Unit 2

The summary of fuel debris in Unit 2 and the results of large-scale experiments carried out by Cooperative Laboratories for Advanced Decommissioning Science (CLADS) is described in Figure 16 [1–3,46]. Both TEPCO and CLADS results indicated the fuel debris at the PCV of Unit 2 is derived from the structural elements because the fuel debris in Unit 2 might exist without mixing between the fuel, which is high-density material, and the structural components, which is the low-density material. This tendency is qualitatively the same as the results of the present study.

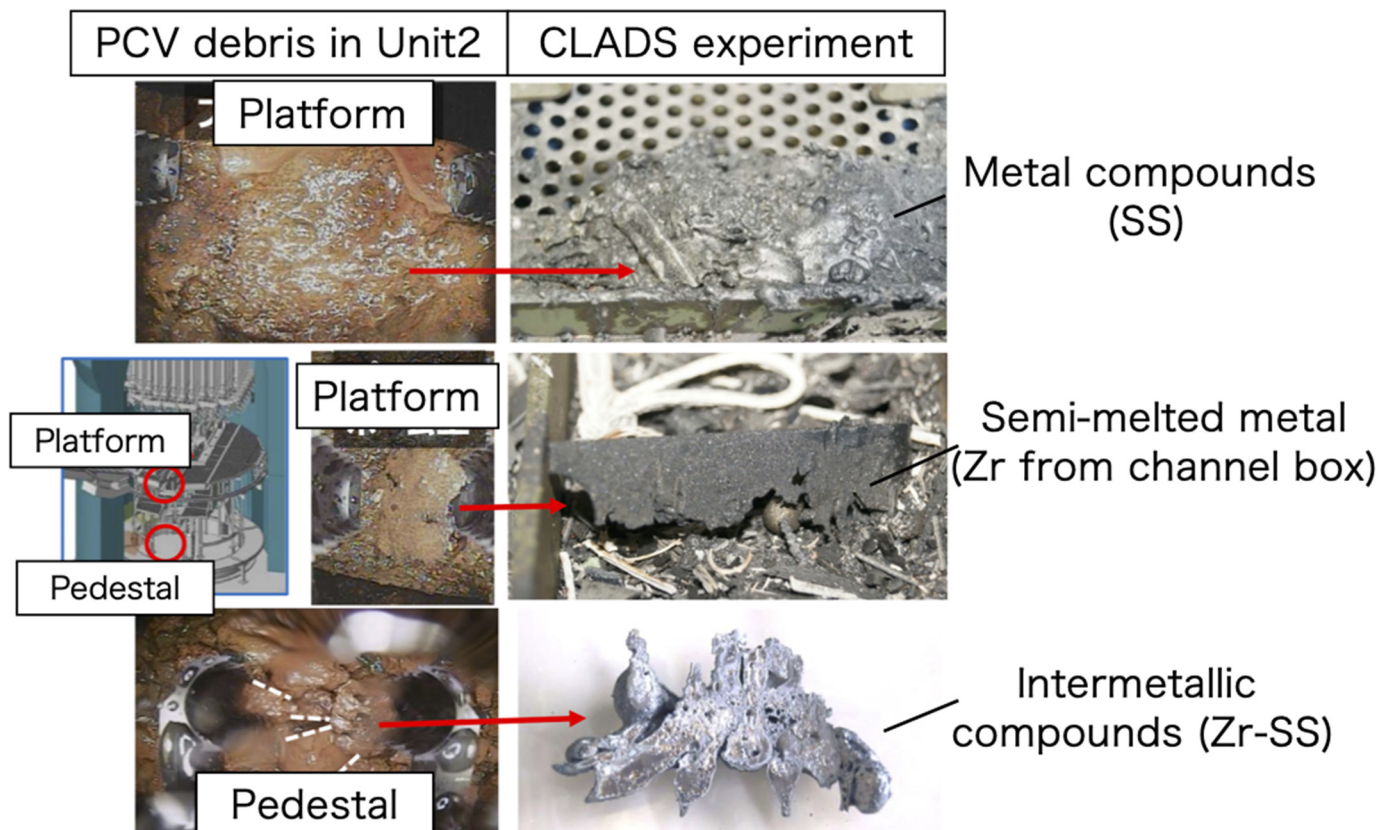


Figure 16. Summary of fuel debris in Unit 2 and the results of large-scale experiments from CLADS [1-3,46].

## 7. Conclusions

The melting-solidification behaviours of the stratified molten metal discharged downward were investigated. The molten metal spreading experiment was performed using two simulant materials with a similar density ratio to the actual fuel and the structural components in Fukushima Daiichi Nuclear Power Plants (1F NPPs). The simulant materials were arranged in the vessel with density and reverse density stratification. The experiments were carried out with various outlet diameters. After the metal spread and solidified, two types of X-ray analysis were conducted. Mapping image analysis was completed to visualize the high-density material distribution in the solidified metal. A point analysis is used to obtain the quantitative values of the high-density material in the solidified metal. Moreover, numerical simulation using the moving particle full-implicit (MPFI) method [31-33], a particle method conserving angular momentum, was performed to reveal the outflow mechanisms and melting-solidification behaviours.

In the experiment with the density stratification, the low-density material accumulated around the centre region on the front side, and the other areas were occupied by the high-density material regardless of the outlet diameters. In the experiment with the reverse density stratification, the material distribution was dependent on the outlet diameters. In specific, the high-density material accumulated around the edge region for the larger outlet. In contrast, with the smaller outlet, the high-density material was deposited around the centre region. According to the existing theoretical estimation, this effect was derived from the inertia effect [44,45].

Numerical simulation was also performed with various outlet diameters to reveal the mechanisms that affect the material distribution after solidification. The simulation results obtained with the density stratification and the reverse density stratification were in good agreement with the experimental mapping image analysis. In the reverse density

stratification, the outflow order and the material distribution after solidification were significantly affected by the outlet diameters.

Overall, the results in this study imply that it is necessary to consider the failure size of the RPV and the mixing/separation condition (e.g., stratification) of the multiple materials in the RPV to understand the fuel debris distribution in 1F NPPs. This is because these conditions may affect the outflow order and the subsequent spreading of the fuel debris.

**Author Contributions:** Conceptualization, R.Y. and S.S.; methodology, R.Y. and M.K.; formal analysis, R.Y. and M.H.; investigation, R.Y.; data curation, R.Y.; writing—original draft preparation, R.Y.; writing—review and editing, M.K.; supervision, M.K., S.S., and K.O. All authors have read and agreed to the published version of the manuscript.

**Funding:** This research received no external funding.

**Institutional Review Board Statement:** Not applicable.

**Informed Consent Statement:** Not applicable.

**Acknowledgments:** This study was partly supported by the Mitsubishi Heavy Industry (MHI). The authors would like to express our gratitude to the members of the MHI committee through meaningful discussion.

**Conflicts of Interest:** The authors declare no conflict of interest.

## References

1. Pshenichnikov, A.; Nagase, Y.; Kurata, M. Comparison of the observed Fukushima Daiichi Unit 2 debris with simulated debris from the CLADS-MADE-01 control blade degradation test. *J. Nucl. Sci. Technol.* **2020**, *58*, 416–425. [[CrossRef](#)]
2. Pschenichnikov, A.; Yamazaki, S.; Bottomley, D.; Nagase, Y.; Kurata, M. Features of a control blade degradation observed in situ during severe accident conditions in boiling water reactors. *J. Nucl. Sci. Technol.* **2019**, *56*, 440–453. [[CrossRef](#)]
3. Pshenichnikov, A.; Kurata, M.; Bottomley, D.; Sato, I.; Nagae, Y.; Yamazaki, S. New research programme of JAEA/CLADS to reduce the knowledge gaps revealed after an accident at Fukushima-1: Introduction of boiling water reactor mock-up assembly degradation test programme. *J. Nucl. Sci. Technol.* **2019**, *57*, 370–379. [[CrossRef](#)]
4. Takano, M.; Nishi, T. High temperature reaction between sea salt deposit and (U,Zr)O<sub>2</sub> simulated corium debris. *J. Nucl. Mat.* **2013**, *443*, 32–39. [[CrossRef](#)]
5. Unit 3 Primary Containment Vessel Internal Investigation. Available online: [http://www.tepco.co.jp/en/nu/fukushima-np/handouts/2017/images/handouts\\_171130\\_03-e.pdf](http://www.tepco.co.jp/en/nu/fukushima-np/handouts/2017/images/handouts_171130_03-e.pdf) (accessed on 26 January 2021).
6. Fukushima Daiichi Nuclear Power Station Unit 2 Primary Containment Vessel Internal Investigation Results. Available online: [http://www.tepco.co.jp/en/nu/fukushima-np/handouts/2018/images/handouts\\_180119\\_01-e.pdf](http://www.tepco.co.jp/en/nu/fukushima-np/handouts/2018/images/handouts_180119_01-e.pdf) (accessed on 26 January 2021).
7. Pellegrini, M.; Dolganov, K.; Herranz, E.; Bonneville, D.; Luxat, D.; Sonnenkalb, M.; Ishikawa, J.; Song, J.H.; Gaunt, R.O.; Fernandez, M.L.; et al. Benchmark Study of the Accident at the Fukushima Daiichi NPS: Best-Estimate Case Comparison. *Nucl. Technol.* **2016**, *196*, 198–210. [[CrossRef](#)]
8. Dinh, T.N.; Kovalikhin, M.J.; Sehgal, B.R. Core Melt Spreading on a reactor Containment Floor. *Prog. Nucl. Energy* **2000**, *36*, 405–468. [[CrossRef](#)]
9. Veteau, J.M. Corine Program, OECD/CSNI/NEA. In Proceedings of the Workshop on Large Molten Pool Heat Transfer, Grenoble, France, 9–11 March 1994; pp. 531–548.
10. Green, G.A.; Finrock, C.; Klages, J.; Schwarzs, C.E.; Burton, S.B. Experimental studies on Melt Spreading, Bubbling Heat Transfer and Coolant Layer Boiling. In Proceedings of the 16th Water Reactor Safety Meeting, NUREG/CP-0097, Gaithersburg, MD, USA, 24 October 1988; pp. 341–358.
11. Suzuki, H.; Matsumoto, T.; Mitadera, T.; Matsumoto, M.; Zama, T. Fundamental experiment and analysis for melt spreading on concrete floor. In Proceedings of the 2nd ASME/JSME Nuclear Engineering Conference 1, San Francisco, CA, USA, 21–24 March 1993; pp. 403–407.
12. Eppinger, B.; Fieg, G.; Schuetz, W.; Stegmaier, U. KATS experiments to simulate corium spreading in the EPR core catcher concept. In Proceedings of the 9th International Conference on Nuclear Engineering (ICONE-9), Nice Acropolis, France, 8–12 April 2001; p. 32068804.
13. Alsmeyer, H.; Cron, T.; Messemer, G.; Häfner, W. ECOKATS-2: A Large Scale Experiment on Melt Spreading and Subsequent Cooling by Top Flooding. In Proceedings of the ICAPP'04 (International Conference Advances in nuclear Power Plants), Pittsburg, KS, USA, 3–17 June 2004; Communication No. 4134.
14. Alsmeyer, H.; Crin, T.; Foit, J.J.; Messemer, G.; Schmidt-Stiefel, S.; Häfner, W.; Kriscio, H. *Test Report of the Melt Spreading Tests ECOKATS-V1 and ECOKATS-1; SAM-ECOSTAR-D15/FZKA 7064; FZKA: Karlsruhe, Germany, 2004.*

15. Steinwarz, W.; Alemberti, A.; Häfner, W.; Alkan, Z.; Fischer, M. Investigations on the phenomenology of ex-vessel core melt behaviour. *Nucl. Eng. Des.* **2001**, *209*, 139–146. [[CrossRef](#)]
16. Tromm, W.; Foit, J.J.; Magallon, D. Dry and wet spreading experiments with prototypic materials at the FARO facility and the theoretical analysis. In Proceedings of the OECD workshop on ex-vessel debris coolability, Karlsruhe, Germany, 15–18 November 1999; FZKA—6475.
17. Journeau, C.; Boccacio, E.; Brayer, C.; Cognet, G.; Hanquet, J.F.; Jégou, C.; Piluso, P.; Moneris, J. Ex-vessel corium spreading: Results from the VULCANO spreading tests. *Nucl. Eng. Des.* **2003**, *223*, 75–102. [[CrossRef](#)]
18. Ogura, T.; Matsumoto, T.; Miwa, S.; Mori, M.; Hibiki, T. Experimental study on molten metal spreading and deposition behaviors. *Ann. Nucl. Energy* **2018**, *118*, 353–362. [[CrossRef](#)]
19. An, S.M.; Song, J.H.; Kim, J.Y.; Kim, H.Y.; Naitoh, M. Experimental Investigation on Molten Pool Representing Corium Composition at Fukushima Daiichi Nuclear Power Plant. *J. Nucl. Mater.* **2016**, *478*, 164–171. [[CrossRef](#)]
20. Ogura, T.; Matsumoto, T.; Miwa, S.; Hibiki, T.; Mori, M. Experimental Study on Molten Metal Spreading and Deposition Behaviors on Wet Surface. *Prog. Nucl. Energy* **2018**, *106*, 72–78. [[CrossRef](#)]
21. Matsumoto, T.; Sakurada, K.; Miwa, S.; Sakashita, H.; Mori, M. Scaling analysis of the spreading and deposition behaviors of molten-core-simulated metals. *Ann. Nucl. Energy* **2017**, *108*, 79–88. [[CrossRef](#)]
22. Sahboun, N.; Miwa, S.; Sawa, K.; Yamamoto, Y.; Watanabe, Y.; Ito, T. A molten metal jet impingement on a flat spreading surface. *J. Nucl. Sci. Technol.* **2020**, *57*, 1111–1120. [[CrossRef](#)]
23. Yokoyama, R.; Suzuki, S.; Okamoto, K.; Harada, M. Scale effect of amount of molten corium and outlet diameters on corium spreading. *Prog. Nucl. Energy* **2020**, *130*, 103535. [[CrossRef](#)]
24. Kang, K.H.; Park, R.J.; Hong, S.H.; Hong, S.W.; Ha, K.S. An experimental study on layer inversion in the corium pool during a severe accident. *Nucl. Eng. Des.* **2014**, *278*, 163–170. [[CrossRef](#)]
25. Li, G.; Oka, Y.; Furuya, M. Experimental and numerical study of stratification and solidification/melting behaviors. *Nucl. Eng. Des.* **2014**, *272*, 109–117. [[CrossRef](#)]
26. Takano, M.; Nishi, T.; Shirasu, N. Characterization of solidified melt among materials of UO<sub>2</sub> fuel and B<sub>4</sub>C control blade. *J. Nucl. Sci. Technol.* **2014**, *51*, 859–875. [[CrossRef](#)]
27. Journeau, C.; Roulet, D.; Porcheron, E.; Piluso, P.; Chagnot, C. Fukushima Daiichi fuel debris simulant materials for the development of cutting and collection technologies. *J. Nucl. Sci. Technol.* **2018**, *55*, 985–995. [[CrossRef](#)]
28. Miwa, S.; Takase, G.; Imoto, J.; Nishioka, S.; Miyahara, N.; Osaka, M. Boron chemistry during transportation in the high temperature region of a boiling water reactor under severe accident. *J. Nucl. Sci. Technol.* **2020**, *57*, 291–300. [[CrossRef](#)]
29. Monaghan, J.J. Simulating free surface flows with SPH. *J. Comput. Phys.* **1994**, *110*, 399–406. [[CrossRef](#)]
30. Koshizuka, S.; Oka, Y. Moving Particle semi-implicit method for fragmentation of incompressible fluid. *Nucl. Sci. Eng.* **1996**, *123*, 421–434. [[CrossRef](#)]
31. Kondo, M. A physically consistent particle method for incompressible fluid flow calculation. *Comput. Part. Mech.* **2021**, *8*, 69–86. [[CrossRef](#)]
32. Kondo, M.; Ueda, S.; Okamoto, K. Melting simulation using a particle method with angular momentum conservation. In Proceedings of the 25th international Conference on Nuclear Engineering ICONE25, Shanghai, China, 2–6 July 2017; p. 67588.
33. Kondo, M. A New Particle Method for Incompressible flow with Thermodynamic Consistency. In Proceedings of the 9th XJTU-UT-SJTU Joint Symposium on Nuclear Science and Technology, Shanghai, China, 13–15 November 2016.
34. Kawahara, T.; Oka, Y. Ex-vessel molten core solidification behavior by moving particle semi-implicit method. *J. Nucl. Sci. Technol.* **2012**, *49*, 1156–1164. [[CrossRef](#)]
35. Chai, P.; Erkan, N.; Kondo, M.; Okamoto, K.; Wei, H. Experimental research and numerical simulation of moving molten metal pool. *Mech. Eng. Lett.* **2015**, *1*, 15-00367. [[CrossRef](#)]
36. Chai, P.; Kondo, M.; Erkan, N.; Okamoto, K. Numerical simulation of MCCI based on MPS method with different types of concrete. *Ann. Nucl. Energy* **2017**, *103*, 227–237. [[CrossRef](#)]
37. Duan, G.; Yamaji, A.; Journeau, C.; Buffe, L.; Haquet, J.F. Investigation on corium spreading over ceramic and concrete substrates in VULCANO VE-U7 experiment with moving particle semi-implicit method. *Ann. Nucl. Energy* **2020**, *141*, 107266. [[CrossRef](#)]
38. Yasumura, Y.; Yamaji, A.; Futruya, M.; Ohishi, Y.; Duan, G. Investigation on influence of crust formation on VULCANO VE-U7 corium spreading with MPS method. *Ann. Nucl. Energy* **2017**, *107*, 119–127. [[CrossRef](#)]
39. Duan, G.; Yamaji, A.; Koshizuka, S. A novel multiphase MPS algorithm for modeling crust formation by highly viscous fluid for simulating corium spreading. *Nucl. Eng. Des.* **2019**, *343*, 218–231. [[CrossRef](#)]
40. Yamaji, A.; Li, X. Development of MPS Method for Analyzing Melt Spreading Behavior and MCCI in Severe Accident. In Proceedings of the 6th Asian Physics Symposium, Bandung, Indonesia, 19–20 August 2015; Volume 739, p. 012002. [[CrossRef](#)]
41. Ramacciotti, M.; Journeau, C.; Sudreau, F.; Cognet, G. Viscosity models for corium melts. *Nucl. Eng. Des.* **2001**, *204*, 377–389. [[CrossRef](#)]
42. Spencer, D.B.; Mehrabian, R.; Flemings, M.C. Rheological behavior of Sn-15 Pct Pb in the Crystallization Range. *Metall. Mater. Trans. B* **1972**, *3*, 1925–1932. [[CrossRef](#)]
43. Joly, P.A.; Mehrabian, R. The rheology of a partially solid alloy. *J. Mater. Sci.* **1976**, *11*, 1393–1418. [[CrossRef](#)]
44. Koyaguchi, T. Magma mixing in a conduit. *J. Volcanol. Geotherm. Res.* **1985**, *25*, 365–369. [[CrossRef](#)]

- 
45. Blake, S.; Ivey, G.N. Magma-mixing and the dynamics of withdrawal from stratified reservoirs. *J. Volcanol. Geotherm. Res.* **1986**, *27*, 153–178. [[CrossRef](#)]
  46. Tokyo Electric Power Company Holdings, Inc. Fukushima Dai-Ichi Nuclear Power Plant Results of Investigation inside Unit 2 PCV. Available online: <https://www.meti.go.jp/earthquake/nuclear/decommissioning/committee/osensuitaisakuteam/2019/02/3-3-3.pdf#page=6> (accessed on 22 April 2021).